

Date of publication xxxx 00, 0000, date of current version xxxx 00, 0000.

Digital Object Identifier 10.1109/ACCESS.2017.Doi Number

# A joint reconstruction and segmentation method for limited-angle X-ray tomography

ZENGHUI WEI<sup>1,2</sup>, BAODONG LIU<sup>1,2</sup>, BIN DONG<sup>3</sup>, LONG WEI<sup>1,2</sup>

<sup>1</sup>Beijing Engineering Research Center of Radiographic Techniques and Equipment, Institute of High Energy Physics, Chinese Academy of Sciences, Beijing 100049, China

<sup>2</sup>School of Nuclear Science and Technology, University of Chinese Academy of Sciences, Beijing 100049, China

<sup>3</sup>Beijing International Center for Mathematical Research, Peking University, Beijing 100871, China

Corresponding author: Baodong Liu (e-mail: liubd@ihep.ac.cn), Bin Dong (e-mail: dongbin@math.pku.edu.cn).

This work was supported by the National Key R&D Program of China 2017YFF0107201 and SRF for ROCS, SEM, and also supported by the National Natural Science Foundation of China Grant 91530321.

**ABSTRACT** Limited-angle computed tomography (CT) is common in industrial applications, where incomplete projection data can cause artifacts. For objects made from homogeneous materials, we propose a joint reconstruction and segmentation method (JRSM) that performs joint image reconstruction and segmentation directly on the projection data. We describe an alternating minimization algorithm to solve the resulting optimization problem, and we modify the primal-dual hybrid gradient (PDHG) algorithm for the non-convex piecewise constant Mumford-Shah (PCMS) model, which is a popular approximation model in biomedical image segmentation. The effectiveness of the proposed approach is validated by simulation and by application to actual micro-CT datasets.

**INDEX TERMS** Limited-angle, Mumford-Shah, PCMS, discrete tomography, prior knowledge.

## I. INTRODUCTION

X-ray computed tomography (CT) has been widely used in many fields, from medical imaging to industrial non-destructive testing (NDT). To acquire complete projection data, the scanning trajectory should cover at least a  $\pi$  plus fan angle range for fan-beam CT scan and a  $\pi$  range for parallel-beam CT scan [1], [2]. If the object is scanned with only a limited angle, the projection data are incomplete. Limited-angle CT reconstruction is an ill-posed inverse problem [3]. Classical reconstruction methods, such as the conventional filtered backprojection (FBP) algorithm and the algebraic reconstruction method (ARM) [4]-[7], have well-known performance constraints in limited-angle situations because these methods have difficulty reducing streak (or wedge) artifacts [8]. To stabilize the reconstruction, additional prior knowledge of the reconstructed object, such as smoothness and sparsity, are integrated into the reconstruction procedure as regularized terms. Among these regularized terms, total variation (TV) [9] is one of the most popular regularizations. Encouraged by theories of compressed sensing [10]-[12], most TV-based models [13]-[16] are based on penalizing the  $l_1$  norm of the image gradient. In [13], Sidky et al. developed an algorithm via alternately performing TV minimization and projection onto

convex sets (POCS). Recently, algorithms based on the  $l_0$  norm [17]-[19] have been developed for the limited-angle problem. Wei Yu et al. [18] used variable splitting and the alternating direction method to solve the unconstrained optimization problem with the  $l_0$  norm of the image gradient. Other regularization-based methods include the wavelet transform [20], [21] and the data-driven sparsity-based method [22].

The prior knowledge that the reconstructed images consist of a set of gray values only can be considered in the reconstruction, if the scanned object is composed of different homogeneous materials. To reconstruct a discrete-valued image from a small number of tomographic projections, discrete tomography (DT) [23] was developed. It was originally concerned with binary images only. Later, the research field expanded to include non-binary and multivalued images. Some studies on DT have already been successfully applied to other imaging fields, such as electron tomography (ET) [24], CT [25], and magnetic resonance imaging (MRI) [26].

In the last few decades, several DT algorithms have been proposed for CT applications. Batenburg et al. developed a heuristic algorithm, the discrete algebraic reconstruction technique (DART) [27], which uses the ARM iteratively to

update part of fixed pixels determined by the segmentation result, and requires prior information on the gray values for thresholding. A series of algorithms based on DART were then developed, including projection distance minimization DART (PDM-DART) [28], which can estimate the gray level parameters adaptively; soft DART (SDART) [29], which includes a soft constraint in the subsequent reconstruction step; and modified DART (MDART) [30], which takes the region of homogeneous material as the research object. The above DART-based methods perform reconstruction and segmentation successively, whereby the reconstruction uses the discrete-valued segmentation to update the image. Because the projection data are used only in the reconstruction step, even a small fluctuation (or error) in the reconstruction or segmentation may significantly influence the result.

In recent years, methods based on joint (or simultaneous) reconstruction and segmentation have been shown to be particularly suitable for DT. The reconstruction and segmentation are essentially performed directly on the projection data. For instance, the total variation regularized discrete algebraic reconstruction technique (TVR-DART) [31] minimizes an energy functional, consisting of a data-fitting term and Huber norm, on the gradient of the discrete-valued approximation using the soft segmentation function. Other joint reconstruction approaches rely predominantly on the piecewise constant Mumford-Shah (PCMS) model (or Potts model [32]), which results in a piecewise constant approximation of the image. The Potts model has been used to solve multi-phase image segmentation, or multi-phase labeling problems. In [19], Storah et al. developed a general discretization scheme for the length terms in the Potts model by minimizing an energy functional consisting of the  $l_0$  norm of the image gradient and the fidelity term. Lauze et al. [33] proposed a method based on the Bayesian rationale and PCMS for limited field-of-view shadowed tomographic data, adopting a discrete squared-gradient magnitude to solve the problem easily. However, there are few DT methods that focus on the limited-angle scenario, and their results tend to be dissatisfying.

Therefore, in this paper, we propose a joint reconstruction and segmentation method (JRSM) for limited-angle reconstruction. In JRSM, the PCMS model is used for discrete-valued segmentation. The algorithm used to solve the PCMS model achieves a favorable balance between the accuracy of the segmentation and computational efficiency. An important advantage of our method is that it lends naturally to the concept of joint reconstruction and CS-based reconstruction.

The rest of this paper is organized as follows. In section II, the concepts of limited-angle CT and DT are introduced; convex relaxation for the PCMS model is formally stated; and the algorithm is presented. The proposed method is validated by simulation as well as by application to actual datasets in sections III and IV, respectively. Conclusions and discussion are given at the end of the paper.

## II. METHODS

In this section, we present the JRSM framework for limited-angle image reconstruction in fan-beam CT scans. First, we formulate the problem of interest. Then, we introduce the PCMS model. Finally, an iterative algorithm is proposed to minimize the PCMS model.

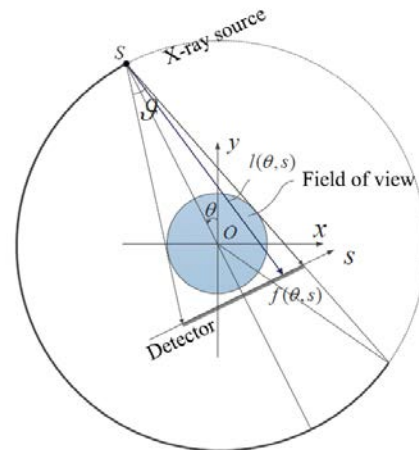


FIGURE 1. Scanning geometry of fan-beam CT scan.

### A. Problem Statement

This work focuses on the fan-beam X-ray CT that is widely used in the NDT of industrial devices. As shown in Fig. 1, assuming the object is stationary, the X-ray source moves along a circular trajectory with the linear detector array. The X-ray is attenuated by the object and collected by the detector. Mathematically, the projection data  $f(\theta, s)$  are obtained from the cone-beam transform of the density function  $u$ ,

$$f(\theta, s) = \int_{\vec{x} \in l(\theta, s)} u(\vec{x}) d\vec{x},$$

where  $u(\vec{x})$  is the linear attenuation coefficient at point  $\vec{x}$ , and  $l(\theta, s)$  represents the line from the X-ray source to the detector element  $s$  at the angle  $\theta$ . The above formula can be viewed as the projection model of the fan-beam CT scan. The task of CT is to recover  $u(\vec{x})$  from the projection data  $f$ . To meet the requirement of an exact reconstruction [34], the range of angle  $\theta$  should be not less than  $\pi$  plus the fan angle  $\vartheta$ . Otherwise, the scan is called limited-angle, and the projection data are incomplete. A discrete version of the projection model can be implemented as a two-dimensional system matrix, which is notated as  $A$  in this article.

We assume the scanned object contains homogeneous materials. Therefore, the reconstruction problem is to find a discrete labeling  $C = \{c_1, c_2, \dots, c_K\}$  for an image  $u$  by solving the following problem:

$$Au = f, \text{ s.t. } u \in C^N,$$

where  $N$  is the number of pixels in the discrete image  $u$ , and  $C^N = C \times C \times \dots \times C$ .

### B. Convex Relaxation for PCMS

The fact that the image  $u$  takes values in a small set of gray values implies a favorable probability that the gray values of  $u$  should be constant in some areas, or in other words,  $u$  is piecewise constant.

Image segmentation is one of the foundational problems in computer vision. Image segmentation is the task of finding appropriate image partitions to form a set of nonoverlapping regions the union of which is the entire image [35]. There are three main approaches to this problem: boundary-based methods (or edge-based methods), region-based methods, and hybrid methods [36]. A celebrated region-based image segmentation model was introduced by Mumford and Shah in 1989 [37]. The Mumford-Shah model consists of the minimization of an energy functional given by

$$\min_{I, S_u} \int_{\Omega} (u - I)^2 dx + \lambda \int_{\Omega \setminus S_u} |\nabla u|^2 dx + \gamma |S_I|, \quad (1)$$

where  $u$  is the real-valued image function on the domain  $\Omega \subset \mathbb{R}^2$ ;  $S_u$  is a discontinuity set in  $\Omega$ ; and  $\gamma$  and  $\lambda$  are the tuning parameters. This model aims to approximate the input image  $u$  in terms of a piecewise smooth function  $I: \Omega \subset \mathbb{R}^2$ , such that  $I$  varies smoothly in each partition and exhibits sharp variations across partition boundaries.

The PCMS model is a variant of the Mumford-Shah model that sets the weighting parameter  $\lambda$  for the middle term in (1) to  $+\infty$ . The approximation  $I$  is forced to become smoother and smoother outside of  $S_u$  with increasing  $\lambda$ . In the limit  $\lambda \rightarrow +\infty$ ,  $I$  is restricted to be piecewise constant, and we obtain the piecewise constant approximation of  $u$ . The PCMS model can be written as the following optimization problem:

$$\min_{\Omega_i, c_i} \sum_{i=1}^K \gamma |\partial\Omega_i| + \int_{\Omega_i} (u - c_i)^2, \quad (2)$$

$$s.t. \quad \bigcup_{i=1}^K \Omega_i = \Omega, \quad \Omega_s \cap \Omega_t = \emptyset, \quad \forall s \neq t,$$

where  $|\partial\Omega_i|$  denotes the perimeter of  $\Omega_i$ . Here,  $c_i \in \mathbb{R}$  is the mean value of the image in the region  $\Omega_i$ , and the parameter  $\gamma$  is used to balance the data-fitting term and the length term. That is, the PCMS model finds a disjointed partition of  $\Omega$  such that  $u$  equals a constant  $c_i$  in  $\Omega_i$ . To solve the above model, the labeling function  $v_i$  is introduced into (2), and the length term is reformulated as

$$\sum_{i=1}^K \gamma |\partial\Omega_i| = \sum_{i=1}^K \gamma \int_{\Omega} |\nabla v_i|,$$

where  $v_i$  for  $i = 1, \dots, K$  is defined as

$$v_i(x) = \begin{cases} 1 & \text{if } x \in \Omega_i, \\ 0 & \text{otherwise.} \end{cases}$$

This allows us to rewrite (2) as

$$\min_{\Omega_i, c_i} \sum_{i=1}^K \gamma \int_{\Omega} |\nabla v_i| + \int_{\Omega_i} v_i (u - c_i)^2,$$

$$s.t. \quad v_i \in \{0, 1\}, \quad \sum_{i=1}^K v_i = 1;$$

$$\bigcup_{i=1}^K \Omega_i = \Omega, \quad \Omega_s \cap \Omega_t = \emptyset, \quad \forall s \neq t.$$

Finally, the discrete version of the PCMS model is reformulated as

$$\min_{v_i, c_i} \gamma \sum_{i=1}^K |\nabla v_i| + \sum_{i=1}^K \langle v_i, (u - c_i)^2 \rangle, \quad (3)$$

$$s.t. \quad v_i \in \{0, 1\}, \quad \sum_{i=1}^K v_i = 1.$$

However, the cost function is non-smooth and non-convex because of the binary constraint on  $v_i$ . Referring to the approach proposed for solving the Potts model in [38]-[40], a convex relaxation is achieved by relaxing  $v_i \in [0, 1]$ , and the model can then be solved by alternating the minimization of the variables  $v_i$  and  $c_i$ , where  $c_i$  can be directly solved by computing

$$c_i = \frac{u^T v_i}{e^T v_i}, \quad e = (1, \dots, 1)^T. \quad (4)$$

Let

$$F(\nabla v) = \gamma \sum_{i=1}^K |\nabla v_i|, \quad g_i = (u - c_i)^2, \quad \langle v, g \rangle = \sum_{i=1}^K \langle v_i, g_i \rangle, \quad (5)$$

where  $v = \{v_1, v_2, \dots, v_K\}$  and  $g = \{g_1, g_2, \dots, g_K\}$ . The relaxation model can be written as

$$\min_{v \in \mathcal{S}} F(\nabla v) + \langle v, g \rangle + \delta_{\mathcal{S}}(v), \quad (6)$$

where  $\mathcal{S}$  is defined as

$$\mathcal{S} = \{v : \Omega \mapsto \mathbb{R}^2 | v_i(x) > 0, \text{ for } 1 \leq i \leq K;$$

$$\sum_{i=1}^K v_i(x) = 1, \forall x \in \Omega\},$$

and  $\delta_{\mathcal{S}}$  is the indicator function of convex set  $\mathcal{S}$ , i.e.,

$$\delta_{\mathcal{S}}(v) = \begin{cases} 0 & \text{if } v \in \mathcal{S}, \\ \infty & \text{otherwise.} \end{cases}$$

Let  $G(v) = \langle v, g \rangle + \delta_{\mathcal{S}}(v)$ ; then, the primal-dual formulation of (6) is given by

$$\min_{v \in \mathcal{S}} \max_p \langle \nabla v, p \rangle + G(v) - F^*(p), \quad (7)$$

where  $p = \{p_1, p_2, \dots, p_K\}$ , and each  $p_k$  corresponds to a dual variable of  $v_k$ . Based on the fact that the conjugate of the norm function is the indicator function of the (unit)

dual-norm ball, we can derive the conjugate function  $F^*(p)$  as

$$F^*(p) = \delta_{C_\gamma}(p),$$

where  $C_\gamma$  is defined as

$$C_\gamma := \{p : \Omega \mapsto \mathbb{R}^2 \mid \|p\|_\infty \leq \gamma, p_n|_{\partial\Omega} = 0\}.$$

The algorithm for solving (7) by the modified primal-dual hybrid gradient (PDHG) [40], [41] is

$$\begin{cases} p^{k+1} = \prod_{C_\gamma} (p^k + \tau(\nabla \bar{v}^k)), \\ v^{k+1} = \prod_S (v - \tau'(g + \nabla^* p^{k+1})), \\ \bar{v}^{k+1} = 2v^{k+1} - v^k, \end{cases} \quad (8)$$

where  $\prod$  is the projection operator onto a convex set.

Here, we have omitted details of the derivation, and interested readers can refer to [38], [39], [42] for more further information. The projection  $\prod_{C_\gamma}$  in (8) can be

rewritten as:

$$\prod_{C_\gamma} x = \gamma \prod_{C_1} \frac{x}{\gamma}.$$

There are multiple ways to discretize the TV term (see [40] for the isotropic case and [43] for the anisotropic case). As for  $\prod_S$ , projection onto a simplex is achieved by the

algorithm presented in [44]. The result  $v_i$  may not be binary because of the convex relaxation. Thus, a truncation procedure that takes the first maximum as 1 and the rest as 0 should be executed after the algorithm converges. The aforementioned procedure for solving (3) is summarized in Algorithm 1.

---

#### Algorithm 1 Multi-phase segmentation method

---

**Input:** Image  $u$ , number of classes  $K$ , parameter  $\gamma$ .

**Output:** Segmentation  $v, c$  of  $u$

1: **Initialization:** Use the K-mean algorithm to produce  $c^0$  from  $u$ . Compute  $g$  by (5). Choose  $\tau > 0$ ,  $\tau' > 0, N_1 > 0$ .

2: **for**  $k \leftarrow 0, N_1$  **do**

3:     Compute  $v^k$  using (8).

4:     Compute  $c^k$  using (4).

5: **end for**

6: Binarize  $v^{N_1}$ .

---

### C. Proposed Joint Reconstruction and Segmentation Method (JRSM)

Considered the inconsistencies between the measurements and the desired data conditions caused by the measurement

errors, scatter, and noise, the limited-angle problem can be modeled by following the discrete linear system

$$f = Au + \eta.$$

This is an underdetermined system of linear equations, which means that limited-angle image reconstruction is an ill-posed linear inverse problem [45], [46]. In 1944, the Levenberg-Marquardt (LM) method, also called the damped least squares (DLS) method, was introduced as the following minimization problem to modify the eigenvalues of the matrix from the normal equation:

$$\min_u \|Au - f\|_2^2 + \tau \|u\|_2^2,$$

where the first term is an  $l_2$  data-fidelity term used to penalize the differences between the measurements and the ideal estimate, and the second term is a regularization term that enforces a small image norm. The regularization parameter  $\tau$  weights the data-fidelity term and the regularization term. Since Tikhonov and Arsenin first proposed the concept [47], introducing regularization to the energy functional has been a common practice to overcome the ill-posed characteristic of inverse problems.

In this paper, we propose the following JRSM by combining (3) with TV-based regularization for CT imaging:

$$\begin{aligned} \min_{v_i, c_i, u} \quad & \gamma \sum_{i=1}^K |\nabla v_i| + \sum_{i=1}^K \langle v_i, (u - c_i)^2 \rangle + \nu \|\nabla u\|_1 \\ & + \frac{\mu}{2} \|Au - f\|_2^2, \end{aligned} \quad (9)$$

$$s.t. \quad v_i \in \{0, 1\}, \quad \sum_{i=1}^K v_i = 1,$$

where  $\gamma, \nu$ , and  $\mu$  are tuning parameters. Now, we briefly describe how (9) can be solved. First, (9) can be split into two sub-problems and solved in an alternating fashion:

$$u^{k+1} = \arg \min_u \sum_{i=1}^K \langle v_i, (u - c_i)^2 \rangle + \frac{\mu}{2} \|Au - f\|_2^2 + \nu \|\nabla u\|_1, \quad (10)$$

$$(v_i^{k+1}, c_i^{k+1}) = \arg \min_{v_i, c_i} \gamma \sum_{i=1}^K |\nabla v_i| + \sum_{i=1}^K \langle v_i, (u^{k+1} - c_i)^2 \rangle,$$

$$s.t. \quad v_i \in \{0, 1\}, \quad \sum_{i=1}^K v_i = 1. \quad (11)$$

The subproblem (10) can be efficiently solved by the Split Bregman algorithm [48] or the alternating direction method of multipliers (ADMM) [49]–[51] as follows:

$$\begin{cases} u^{k+1} = (\mu A^T A + 2I - \lambda \Delta)^{-1} (\lambda \nabla^* (\alpha^k - b^k) \\ \quad \quad \quad + \mu A^T f + 2 \sum_{i=1}^K v_i \cdot c_i), \\ \alpha^{k+1} = \mathcal{T}_{\nu/\lambda} (\nabla u^{k+1} + b^k), \\ b^{k+1} = b^k + \sigma (\nabla u^{k+1} - \alpha^{k+1}). \end{cases} \quad (12)$$

Here,  $\mathcal{T}_{\nu/\lambda}$  is the soft-thresholding operator [52]–[54]:

$$\mathcal{T}_{\nu/\lambda}(s) = \left\{ 1 - \frac{\nu}{\lambda|s|} \right\}_+ s.$$

The subproblem (11) is the same as (3), which can be efficiently solved by Algorithm 1.

Algorithm 2 is presented for the proposed JRSM. Either the segmentation result  $\sum_{i=1}^K v_i \cdot c_i$  or  $u_i$  can be taken as the output of the algorithm.

---

**Algorithm 2** JRSM for limited-angle CT

---

**Input:** Sinogram  $f$ , system matrix  $A$ , number of classes  $K$ , weighting parameters  $\gamma, \mu, \nu$ .

**Output:** Reconstruction  $u$  and segmentation  $v, c$  of  $u$

- 1: **Initialization:** Set  $u^0 = 0, i = 0, N_2 > 0$  and  $\epsilon > 0$ .
  - 2: **repeat**
  - 3:     Solve for  $v^i, c^i$  from  $u^i$  by Algorithm 1.
  - 4:     Solve for  $u^{i+1}$  from  $v^i, c^i$  and  $u^i$
  - 5:     **for**  $l \leftarrow 0, N_2$  **do**
  - 6:         Update  $u^{i(l)}$  by (12).
  - 7:     **end for**
  - 8:      $i \leftarrow i + 1$
  - 9: **until.**  $\|u^{i+1} - u^i\|_2^2 < \epsilon$
- 

### III. NUMERICAL EVALUATION

Here, we present a series of simulations to test the performance of the proposed JRSM. All the simulations were implemented in MATLAB on a laptop with 1.8 GHz Intel Xeon E5-2603 CPU processors. As shown in the first row of Fig. 2, the simulations were based on a set of three images (*Sponge*, *Bone*, and *FORBILD* head phantom), with sizes of  $128 \times 128$  pixels. The *Sponge* image was binary and represented a cross-section of collagen sponges [55]. The *Bone* image we simulated had three gray levels and represented a cross-section of cancellous bone. The *FORBILD* head phantom [56], which contains four gray levels, is widely used by researchers working on two-dimensional (2D) image reconstruction. The simulated geometrical scanning parameters were as follows: the source-detector distance (SDD) was 1536 mm, the source-to-object (SOD) distance was 512 mm, the pixel size of the object was 1 mm, and there were 300 detector elements with sizes of 2 mm.

The peak signal-to-noise ratio (PSNR) defined as (13), the relative mean error (RME) given in formula (14), and the structural similarity (SSIM) defined in [57] were used to measure the quality of the reconstructed images:

$$PSNR: = -10 \log_{10} \frac{\|u - \tilde{u}\|_2^2}{255n}, \quad (13)$$

$$RME: = \frac{\|u - \tilde{u}\|_2}{\|u\|_2}, \quad (14)$$

where  $\tilde{u}$  is the original designed phantom, and  $u$  is the reconstructed image. The relative mean accuracy (RMC) is defined as

$$RMC: = 1 - \frac{\|u - \tilde{u}\|_2}{\|u\|_2}, \quad (15)$$

in this paper.

#### A. Noise-Free Projection Data

We first conducted simulations to evaluate the reconstruction performance of the proposed method on noise-free radon projection data, which contained 90 angles equally distributed across  $90^\circ$  of angular scanning. Fig. 2 shows the reference images (first row) and results of the simultaneous iterative reconstruction technique (SIRT) [7], TVR-DART, and the proposed algorithm. SIRT is an algebraic reconstruction method used to solve linear systems and proven to converge to a solution of the weighted least squares problem associated with the linear system [58]. The reconstruction parameters for TVR-DART and JRSM are listed in Table I. The differences relative to the phantoms are shown in Fig. 3. The streak artifacts in the SIRT results were the severest and mainly appeared on the edges along the missing X-rays. The streak artifacts were suppressed by both the TVR-DART and the JRSM. However, the JRSM performed better than the TVR-DART, especially in the region near the edge of the images. In the JRSM results, both the structure and the consistency of the gray values were reconstructed well.

In addition to the graphical comparisons, performance metrics for all of the above reconstructions are reported in Table II. The JRSM generally outperformed SIRT and TVR-DART, except that the SSIM used in the JRSM on the binary *Sponge* image was slightly smaller than that of the TVR-DART.

This subsection compared the reconstruction quality based on noiseless projection data. In the next subsection, we will verify the robustness of the JRSM with noisy projection data.

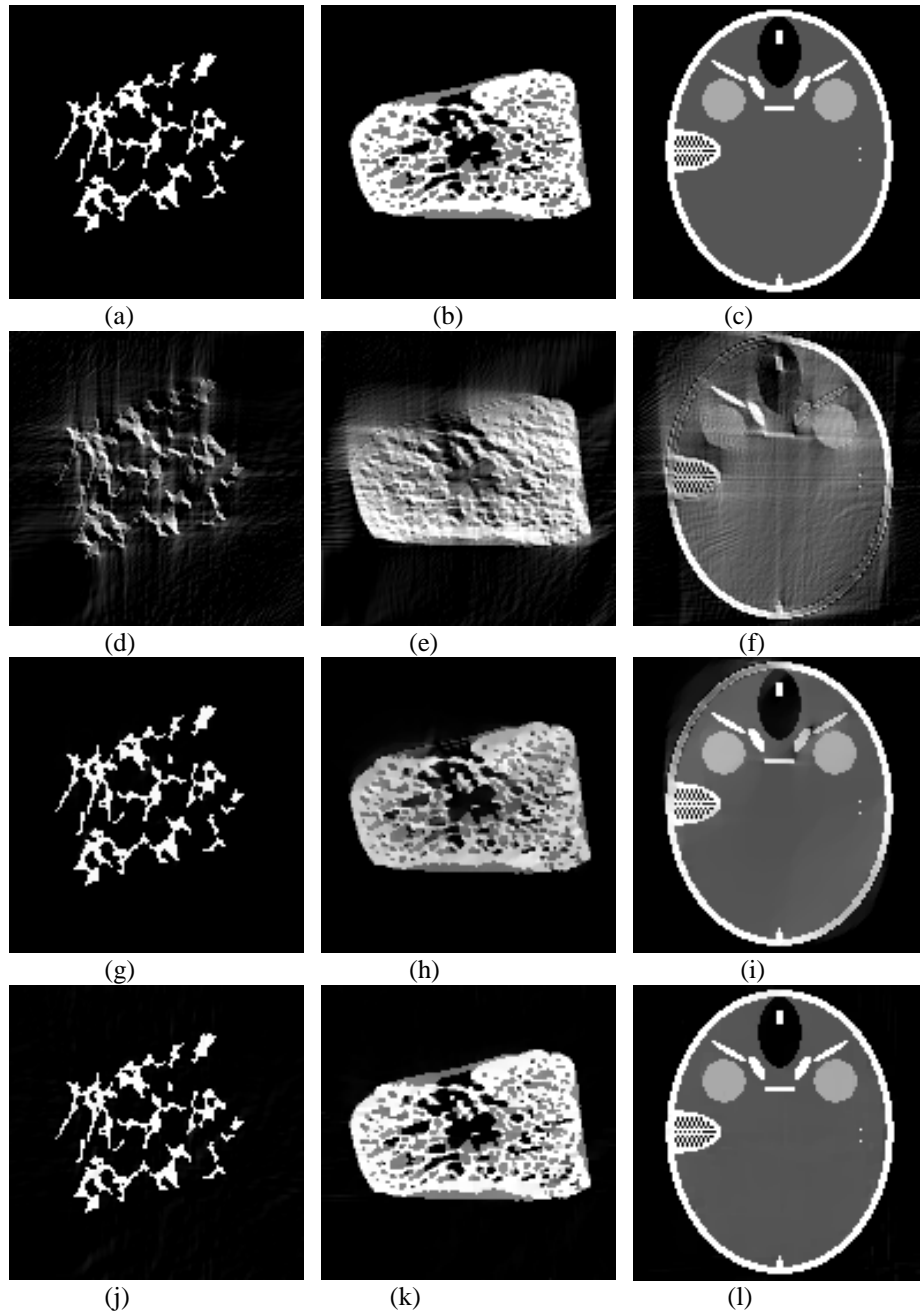


FIGURE 2. Original test images of (a) *Sponge*, (b) *Bone*, and (c) *FORBILD* head used in the simulation experiments for the reconstruction using SIRT (d-f), TVR-DART (g-i), and JRSM (j-l). The left, middle, and right columns show the display windows [0, 1], [0, 2], and [0, 3], respectively.

TABLE I  
RECONSTRUCTION PARAMETERS FOR TVR-DART AND JRSM ON THE NOISE-FREE PROJECTIONS

Phantom	TVR-DART		JRSM		
	weighting parameter	$\gamma$	$\mu$	$\nu$	
<i>Sponge</i>	10	0.01	0.82	2.2	
<i>Bone</i>	6	0.01	0.5	2	
<i>FORBILD</i>	2	0.1	0.8	3	

TABLE II  
EVALUATIONS OF THE RESULTS RECONSTRUCTED FROM NOISE-FREE PROJECTIONS BY DIFFERENT ALGORITHMS

Phantom	PSNR			RME			SSIM		
	SIRT	TVR-DART	JRSM	SIRT	TVR-DART	JRSM	SIRT	TVR-DART	JRSM
<i>Sponge</i>	64.8189	87.7613	87.8000	0.5811	0.0414	0.0412	0.3633	0.9888	0.9717
<i>Bone</i>	58.2201	65.7135	72.3460	0.3503	0.1478	0.0688	0.4221	0.8544	0.8623
<i>FORBILD</i>	54.7920	61.8061	74.5094	0.3992	0.1780	0.0412	0.2991	0.8923	0.9141

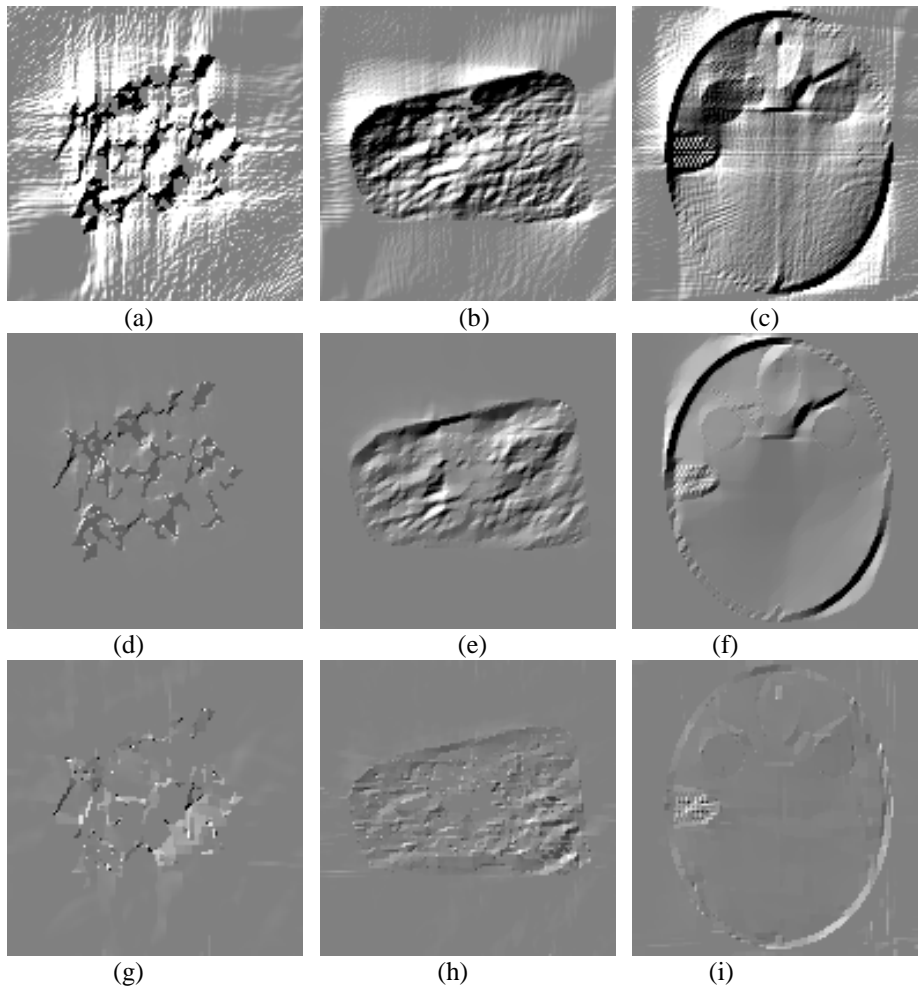


FIGURE 3. Differences between the reconstructed results from SIRT, TVR-DART, and JRSJ in Fig. 2, and the corresponding original phantom image. The left, middle, and right columns show the display windows  $[-0.1, 0.1]$ ,  $[-0.6, 0.6]$ , and  $[-0.6, 0.6]$ , respectively.

### B. Projection Data with Noise

The simulation of the noisy projection followed the method presented in [59]. Poisson noise was considered in our experiments. First, the projection data were generated by taking the exponentials of the negative values of the normalized noise-free sinogram, which was obtained by dividing the noise-free sinogram by its maximum value  $f_m$ . The noise-free sinogram was then perturbed with Poisson-distributed noise assuming a maximum number of photon counts  $I_0$  for the detectors bins. In these simulations,  $I_0$  was given three values,  $1 \times 10^4$ ,  $5 \times 10^4$ , and  $1 \times 10^5$ , to study the algorithms' performances at different noise levels ( $1 \times 10^5$  is commonly used in medical studies on low-dose reconstruction [60]). The three levels were classified as high, medium, and low noise, respectively. Finally, the noisy sinogram was obtained by multiplying the original sinogram maximum value  $f_m$  by the negative logarithm transform of the noisy projection data.

Fig. 4 shows the JRSJ's reconstructed results from the noisy projection data. For *Sponge*, the reconstruction was nearly perfect, even with high-level noise. For *Bone* and *FORBILD*, the results were influenced by noise; however, most details were well-preserved. All of the results improved with decreased noise levels. It is also supported by PSNRs, RMEs, and SSIMs. In addition, Fig. 5 demonstrates the convergence of the RMEs in the reconstructions of all three phantoms with all three different noise levels: the algorithm converged after approximately 20 iterations in all cases.

The JRSJ's reconstruction parameters  $\gamma$ ,  $\mu$ , and  $\nu$  are listed in Table IV. The robustness of the parameters was mainly due to the simplicity of the image phantoms, as well as the fact that the PCMS model is robust to noise and the segmentation result does not vary too much with slight changes of  $\gamma$ . In addition, choosing an appropriate value based on the segmentation performance is helpful before doing the reconstruction. As for the data-fidelity parameter  $\mu$  and the TV parameter  $\nu$ , improving the ratio of  $\nu$  is a reasonable expectation in cases of increased noise levels.

Hence, these simulations of noisy projection data demonstrated that the proposed algorithm produces high-quality results, favorable robustness, and fast convergence in

the reconstruction of noisy projection data from limited-angle CT scans.

TABLE III  
EVALUATIONS OF THE RECONSTRUCTION RESULTS OF PHANTOMS USING PROJECTIONS WITH DIFFERENT LEVELS OF POISSON NOISE

PHANTOM	PSNR			RME			SSIM		
	High	Medium	Low	High	Medium	Low	High	Medium	Low
<i>SPONGE</i>	81.4488	82.9132	83.4697	0.0856	0.0723	0.0679	0.7589	0.8242	0.8373
<i>BONE</i>	64.0791	67.8341	68.2949	0.1784	0.1158	0.1098	0.5952	0.7306	0.8009
<i>FORBILD</i>	62.8809	68.9311	72.9171	0.1573	0.0784	0.0495	0.4187	0.7139	0.8444

TABLE IV  
JRSR RECONSTRUCTION PARAMETERS FOR PROJECTIONS WITH DIFFERENT LEVELS OF POISSON NOISE

PHANTOM	High			Medium			Low		
	$\gamma$	$\mu$	$\nu$	$\gamma$	$\mu$	$\nu$	$\gamma$	$\mu$	$\nu$
<i>SPONGE</i>	0.01	1	2	0.01	1	2	0.01	1	2
<i>BONE</i>	0.01	0.4	3	0.01	0.5	2	0.01	0.6	2
<i>FORBILD</i>	0.097	1	5	0.1	1.2	5	0.097	1.3	6

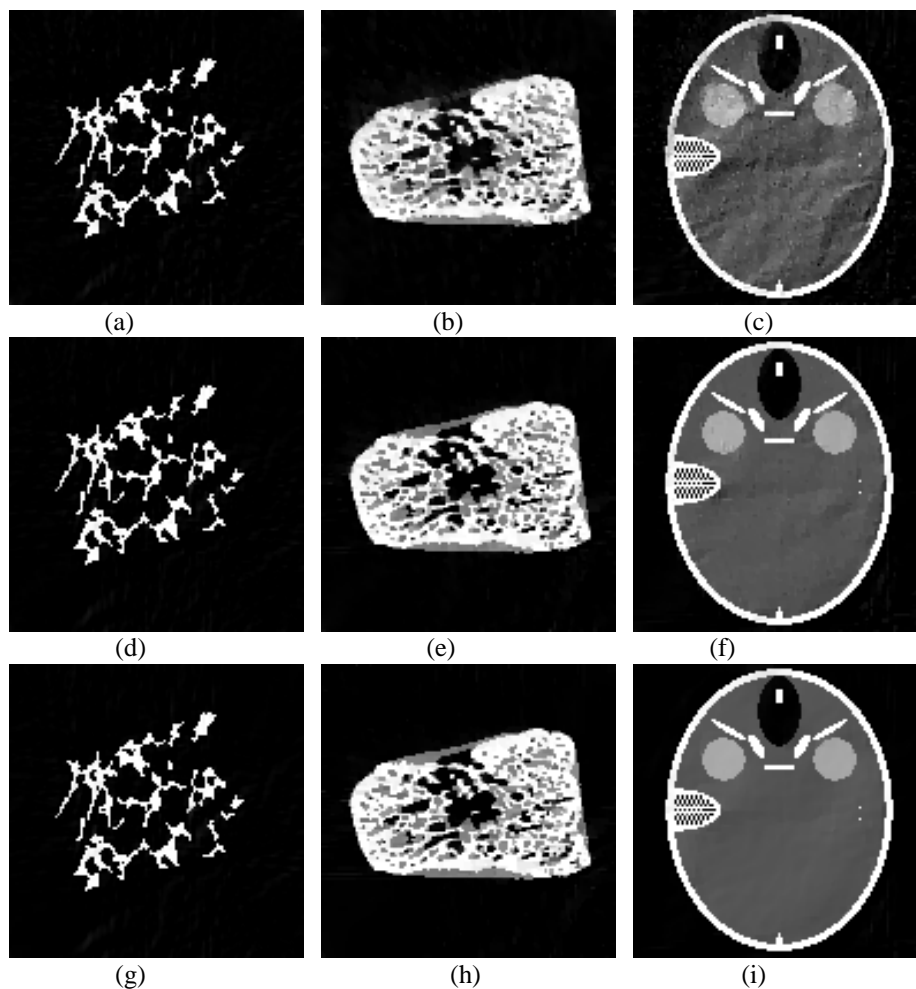


FIGURE 4. Reconstructed results from JRSR for noisy projection data with varying noise levels:  $1 \times 10^4$  photon count (top row),  $5 \times 10^4$  (middle row) and  $1 \times 10^5$  (bottom row). The left, middle, and right columns show the display windows [0, 1], [0, 2], and [0, 3], respectively.

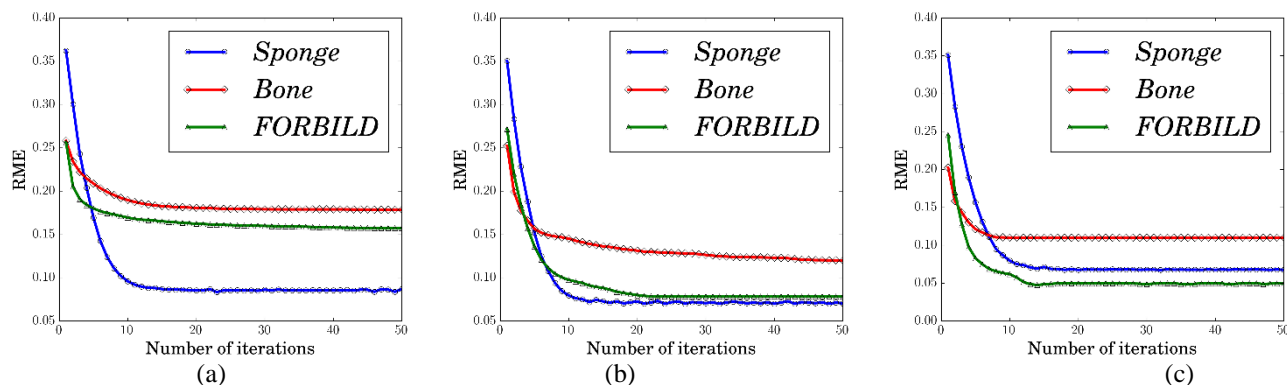


FIGURE 5. The RMEs with respect to the iteration numbers with three noise levels: (a)  $1 \times 10^4$ , (b)  $5 \times 10^4$  and (c)  $1 \times 10^5$  photon counts.

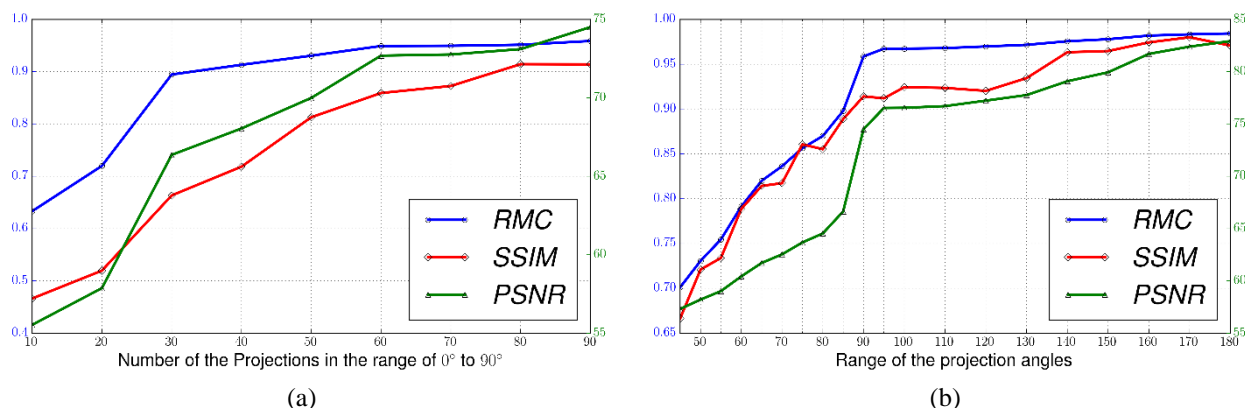


FIGURE 6. (a) RMC, SSIM, and PSNR with respect to the number of projections in the  $90^\circ$  angle range. (b) RMC, SSIM, and PSNR with respect to the projection angle range varying from  $45^\circ$  to  $180^\circ$ .

### C. Number of Projections and Rotation Angle

In the previous series of simulations, 90 projections were taken, uniformly distributed across the range of  $90^\circ$ . This subsection presents simulations in which the number of projections and the rotation angle were altered to further test the JRSM performance. Only the *FORBILD* head phantom was used in these experiments.

Fig. 6a shows the RMC, SSIM, and PSNR values with respect to the number of projections in the angle range of  $90^\circ$  (from  $0^\circ$  to  $90^\circ$ ), varying from 10 to 90. As expected, the higher the projection number, the larger the RMC values. Along with the increased number of projections, the RMC curve changed from ragged to flat. This result indicates that the JRSM requires a minimum number of projections to maintain the reconstruction quality, such as 30 projections in this case. Furthermore, the tendencies of the SSIM and PSNR curves were basically consistent with the RMC curve.

Fig. 6b shows the RMC, SSIM, and PSNR values with respect to the projection angle range, varying from  $45^\circ$  to  $180^\circ$ . Here, the angular sampling was uniform with intervals of  $1^\circ$ . Therefore, the number of projections increased linearly with the angular range. The curves in Fig. 6b present similar behavior as the ones in Fig. 6a. The JRSM worked well when the rotation angle was larger than  $90^\circ$ .

As demonstrated by Fig. 6, the JRSM exhibits favorable performance as long as the number of projections and the rotation angle reaches a minimum limit.

## IV. EXPERIMENTAL VERIFICATION

To further evaluate the proposed algorithm under practical conditions, we applied the algorithm to two real experimental datasets, which were acquired by micro-CT scans consisting of a  $1024 \times 768$  pixel detector with pixel sizes of  $194 \mu\text{m}$  and an X-ray tube with a maximum voltage of 225 kV. In the following experiments, only the data from the central row of the detector were extracted to form a fan-beam CT image. The SIRT's reconstructed results from completed projection data were used as the ground truth of the scanning objects.

### A. PCB Data

The first specimen was cut from a piece of printed circuit board (PCB). There were metal rings immediately adjacent to holes filled with air in the board. The specimen was scanned with X-rays with a maximum energy of 140 keV. Data from 360 evenly spaced projections covering  $[0^\circ, 360^\circ)$  were collected. The ground truth in this experiment is shown in Fig. 7a. The interior of the metal rings is filled with air. However, because of beam hardening and scatter, their

values were not zeroes. Fig. 7b and Fig. 7c show the reconstructions from the TVR-DART and JRSM using the first 150 projections in the range of  $[0^\circ, 150^\circ)$ . Compared to TVR-DART, the JRSM reconstruction was smoother, and the wedge artifacts were suppressed. The difference between Fig. 7a and Fig. 7c is shown in Fig. 7d, where we can see that the proposed algorithm reconstructed most of the phantom details except its boundaries.

### B. Phantom Data

The phantom was composed of four quarter cylinders with holes of the same size. As shown in Fig. 7e, an iron wire was put into the hole in the upper-left region, and the hole in the lower-right region was filled with an aluminum rod. The other two holes were filled with air. Apart from the air, the

phantom contained two other materials: the aluminum used in the two quarters with empty holes, and plexiglass in the rest. The ground truth contained some artifacts near the iron wire because of beam hardening and scatter. Data from 720 projections from  $0^\circ$  to  $360^\circ$  with  $0.5^\circ$  increments were collected, and a series of the first 300 projections were taken as the limited-angle reconstruction dataset. From Fig. 7f and Fig. 7g, the upper-left of the image was difficult to reconstruct because of beam hardening and scatter. Compared to the result from TVR-DART shown in Fig. 7f, the JRSM performed better, especially near the iron wire. From the difference between the JRSM and the ground truth images shown in Fig. 7e, the JRSM exhibited favorable performance except near the iron wire.

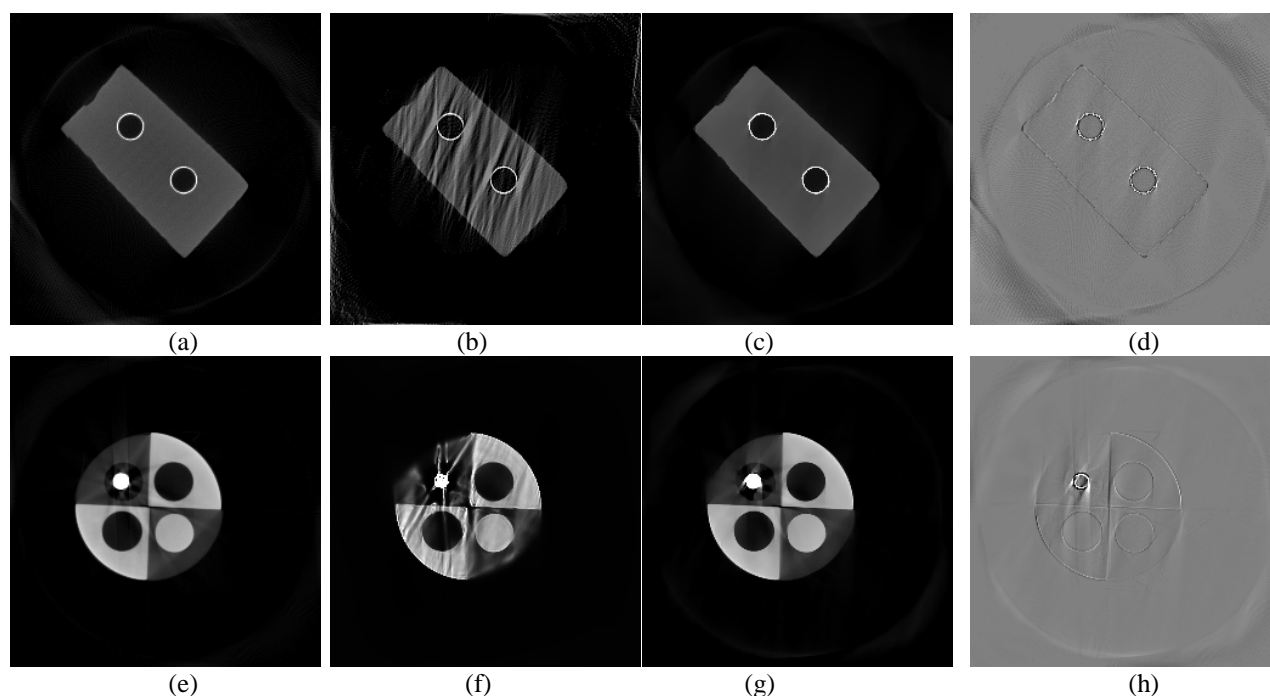


FIGURE 7. Top row: Experimental results with PCB specimen. Bottom row: Experimental results with phantom. Left column: Ground truth reconstructed from completed projection data using SIRT. 2nd and 3rd columns: Reconstructed results from TVR-DART and JRSM over a rotation angle of  $150^\circ$ . Right column: Differences between JRSM results and the corresponding ground truth. The display windows of the first row were set to  $[0, 7]$ , except (d) is set to  $[-2, 2]$ ; the display windows of the second row were set to  $[0, 5]$ , except (h) is set to  $[-2, 2]$ .

## V. CONCLUSIONS

In this paper, we proposed a joint reconstruction and segmentation model, JRSM, for limited-angle CT scans, which can be applied to imaging objects made from homogeneous materials. We developed and implemented an alternating minimization algorithm for the proposed JRSM. The algorithm alternately solves two subproblems. One of the subproblem is a convexified piecewise Mumford-Shah model, which is solved using a modified PDHG algorithm. The other subproblem is a standard convex image restoration model that is solved efficiently using the split

Bregman/ADMM algorithm. Compared to existing methods that alternately perform segmentation and update the reconstruction image, the proposed JRSM method jointly performs image reconstruction and segmentation directly on the projection data. The reconstruction coupled with segmentation is more robust and efficient than alternating methods. Numerical simulations with three phantoms were conducted using noiseless projection data and projection data corrupted by three different levels of Poisson noise. Simulations were also conducted with different numbers of projections and different rotation angles to demonstrate the performance of the proposed method. Two real experimental

datasets acquired by micro-CT scans were further used to demonstrate the superiority of the proposed method in practical scenarios. All results showed that the proposed method is effective in limited-angle image reconstruction. However, the current implementation of the proposed algorithm is time-consuming. It taken about 60 minutes to get Fig. 7c. Our future work will focus on speeding the JRSM reconstruction process.

## ACKNOWLEDGMENT

The authors would like to thank Pengfei Yin from the Institute of Vertebrate Paleontology and Paleoanthropology, Chinese Academy of Sciences (IVPP-CAS) for providing the CT scan used in this study.

## REFERENCES

- [1] D. L. Parker, "Optimal short scan convolution reconstruction for fan beam ct," *Medical physics*, vol. 9, no. 2, pp. 254–257, 1982.
- [2] F. Noo, M. Defrise, R. Clackdoyle, and H. Kudo, "Image reconstruction from fan-beam projections on less than a short scan," *Physics in Medicine and Biology*, vol. 47, no. 14, p. 2525, 2002.
- [3] F. Natterer, "The limited angle problem," in *The mathematics of computerized tomography*. SIAM, 2001, vol. 32, pp. 160–166.
- [4] A. H. Andersen, "Algebraic reconstruction in ct from limited views," *IEEE Trans. Med. Imag.*, vol. 8, no. 1, pp. 50–55, 1989.
- [5] R. Gordon, R. Bender, and G. T. Herman, "Algebraic reconstruction techniques (art) for three-dimensional electron microscopy and x-ray photography," *Journal of theoretical Biology*, vol. 29, no. 3, pp. 471N1477–476N2481, 1970.
- [6] A. H. Andersen and A. C. Kak, "Simultaneous algebraic reconstruction technique (sart): a superior implementation of the art algorithm," *Ultrasonic imaging*, vol. 6, no. 1, pp. 81–94, 1984.
- [7] S. Bangliang, Z. Yiheng, P. Lihui, Y. Danya, and Z. Baofen, "The use of simultaneous iterative reconstruction technique for electrical capacitance tomography," *Chemical Engineering Journal*, vol. 77, no. 1, pp. 37–41, 2000.
- [8] J. Frikel and E. T. Quinto, "Characterization and reduction of artifacts in limited angle tomography," *Inverse Problems*, vol. 29, no. 12, p. 125007, 2013.
- [9] L. I. Rudin, S. Osher, and E. Fatemi, "Nonlinear total variation based noise removal algorithms," *Physica D: Nonlinear Phenomena*, vol. 60, no. 1-4, pp. 259–268, 1992.
- [10] D. L. Donoho, "Compressed sensing," *IEEE Trans. Inf. Theory*, vol. 52, no. 4, pp. 1289–1306, 2006.
- [11] E. J. Candes, Y. C. Eldar, D. Needell, and P. Randall, "Compressed sensing with coherent and redundant dictionaries," *Applied and Computational Harmonic Analysis*, vol. 31, no. 1, pp. 59–73, 2011.
- [12] E. J. Candès, J. Romberg, and T. Tao, "Robust uncertainty principles: Exact signal reconstruction from highly incomplete frequency information," *IEEE Trans. Inf. Theory*, vol. 52, no. 2, pp. 489–509, 2006.
- [13] E. Y. Sidky, C.-M. Kao, and X. Pan, "Accurate image reconstruction from few-views and limited-angle data in divergent-beam ct," *Journal of X-ray Science and Technology*, vol. 14, no. 2, pp. 119–139, 2006.
- [14] Z. Chen, X. Jin, L. Li, and G. Wang, "A limited-angle ct reconstruction method based on anisotropic tv minimization," *Physics in medicine and biology*, vol. 58, no. 7, p. 2119, 2013.
- [15] M. Persson, D. Bone, and H. Elmqvist, "Total variation norm for three dimensional iterative reconstruction in limited view angle tomography," *Physics in Medicine and Biology*, vol. 46, no. 3, p. 853, 2001.
- [16] X. Jin, L. Li, Z. Chen, L. Zhang, and Y. Xing, "Anisotropic total variation for limited-angle ct reconstruction," in *Nuclear Science Symposium Conference Record (NSS/MIC)*, 2010 IEEE. IEEE, 2010, pp. 2232–2238.
- [17] S. Yu-Li and T. Jin-Xu, "Image reconstruction from few views by l0-norm optimization," *Chinese Physics B*, vol. 23, no. 7, p. 078703, 2014.
- [18] W. Yu, C. Wang, and M. Huang, "Edge-preserving reconstruction from sparse projections of limited-angle computed tomography using l0-regularized gradient prior," *Review of Scientific Instruments*, vol. 88, no. 4, p. 043703, 2017.
- [19] M. Storath, A. Weinmann, J. Frikel, and M. Unser, "Joint image reconstruction and segmentation using the potts model," *Inverse Problems*, vol. 31, no. 2, p. 025003, 2015.
- [20] M. Rantala, S. Vanska, S. Jarvenpaa, M. Kalke, M. Lassas, J. Moberg, and S. Siltanen, "Wavelet-based reconstruction for limited-angle x-ray tomography," *IEEE Trans. Med. Imag.*, vol. 25, no. 2, pp. 210–217, 2006.
- [21] M. Bhatia, W. C. Karl, and A. S. Willsky, "A wavelet-based method for multiscale tomographic reconstruction," *IEEE Trans. Med. Imag.*, vol. 15, no. 1, pp. 92–101, 1996.
- [22] J. K. Choi, B. Dong, and X. Zhang, "Limited tomography reconstruction via tight frame and simultaneous sinogram extrapolation," *Journal of Computational Mathematics*, vol. 34, no. 6, pp. 575–589, 2016.
- [23] A. Kuba and G. T. Herman, "Discrete tomography: A historical overview," in *Discrete tomography*. Springer, 1999, pp. 3–34.
- [24] J. R. Jinschek, K. J. Batenburg, H. A. Calderon, R. Kilaas, V. Radmilovic, and C. Kisielowski, "3-d reconstruction of the atomic positions in a simulated gold nanocrystal based on discrete tomography: Prospects of atomic resolution electron tomography," *Ultramicroscopy*, vol. 108, no. 6, pp. 589–604, 2008.
- [25] G. T. Herman and A. Kuba, "Discrete tomography in medical imaging," *Proc. IEEE*, vol. 91, no. 10, pp. 1612–1626, 2003.
- [26] I. Nyström and Ö. Smedby, "Analysis of magnetic resonance angiography images using skeletonization and distance transforms," *Discrete Mathematical Problems with Medical Applications*, vol. 55, pp. 75–89, 2000.
- [27] K. J. Batenburg and J. Sijbers, "Dart: a practical reconstruction algorithm for discrete tomography," *IEEE Trans. Image Process.*, vol. 20, no. 9, pp. 2542–2553, 2011.
- [28] W. van Aarle, K. J. Batenburg, and J. Sijbers, "Automatic parameter estimation for the discrete algebraic reconstruction technique (dart)," *IEEE Trans. Image Process.*, vol. 21, no. 11, pp. 4608–4621, 2012.
- [29] F. Bleichrodt, F. Tabak, and K. J. Batenburg, "Sdart: An algorithm for discrete tomography from noisy projections," *Computer Vision and Image Understanding*, vol. 129, pp. 63–74, 2014.
- [30] Z. Liang, Y. Guan, G. Liu, X. Chen, F. Li, P. Guo, and Y. Tian, "A modified discrete algebraic reconstruction technique for multiple grey image reconstruction for limited angle range tomography," *Journal of synchrotron radiation*, vol. 23, no. 2, pp. 606–616, 2016.
- [31] X. Zhuge, W. J. Palenstijn, and K. J. Batenburg, "Tvr-dart: a more robust algorithm for discrete tomography

- from limited projection data with automated gray value estimation," *IEEE Trans. Image Process.*, vol. 25, no. 1, pp. 455–468, 2016.
- [32] R. B. Potts, "Some generalized order-disorder transformations," in *Mathematical proceedings of the cambridge philosophical society*, vol. 48, no. 1. Cambridge University Press, 1952, pp. 106–109.
- [33] F. Lauze, Y. Quéau, and E. Plenge, "Simultaneous reconstruction and segmentation of ct scans with shadowed data," in *International Conference on Scale Space and Variational Methods in Computer Vision*. Springer, 2017, pp. 308–319.
- [34] H. K. Tuy, "An inversion formula for cone-beam reconstruction," *SIAM Journal on Applied Mathematics*, vol. 43, no. 3, pp. 546–552, 1983.
- [35] R. M. Haralock and L. G. Shapiro, "Image segmentation," in *Computer and robot vision*. Addison-Wesley Longman Publishing Co., Inc., 1991, pp. 509–550.
- [36] K. Haris, S. N. Efstratiadis, N. Maglaveras, and A. K. Katsaggelos, "Hybrid image segmentation using watersheds and fast region merging," *IEEE Transactions on image processing*, vol. 7, no. 12, pp. 1684–1699, 1998.
- [37] D. Mumford and J. Shah, "Optimal approximations by piecewise smooth functions and associated variational problems," *Communications on pure and applied mathematics*, vol. 42, no. 5, pp. 577–685, 1989.
- [38] C. Tai, X. Zhang, and Z. Shen, "Wavelet frame based multiphase image segmentation," *SIAM Journal on Imaging Sciences*, vol. 6, no. 4, pp. 2521–2546, 2013.
- [39] F. Li, M. K. Ng, and C. Li, "Variational fuzzy mumford-shah model for image segmentation," *SIAM Journal on Applied Mathematics*, vol. 70, no. 7, pp. 2750–2770, 2010.
- [40] A. Chambolle and T. Pock, "A first-order primal-dual algorithm for convex problems with applications to imaging," *Journal of mathematical imaging and vision*, vol. 40, no. 1, pp. 120–145, 2011.
- [41] E. Esser, X. Zhang, and T. F. Chan, "A general framework for a class of first order primal-dual algorithms for convex optimization in imaging science," *SIAM Journal on Imaging Sciences*, vol. 3, no. 4, pp. 1015–1046, 2010.
- [42] M. Burger, C. Rossmanith, and X. Zhang, "Simultaneous reconstruction and segmentation for dynamic spect imaging," *Inverse Problems*, vol. 32, no. 10, p. 104002, 2016.
- [43] M. Zhu and T. Chan, "An efficient primal-dual hybrid gradient algorithm for total variation image restoration," *UCLA CAM Report*, vol. 34, 2008.
- [44] C. Zach, D. Gallup, J.-M. Frahm, and M. Niethammer, "Fast global labeling for real-time stereo using multiple plane sweeps," in *VMV*, 2008, pp. 243–252.
- [45] A. G. Ramm, "Inversion of limited-angle tomographic data," *Computers & Mathematics with Applications*, vol. 22, no. 4-5, pp. 101–111, 1991.
- [46] M. E. Davison, "The ill-conditioned nature of the limited angle tomography problem," *SIAM Journal on Applied Mathematics*, vol. 43, no. 2, pp. 428–448, 1983.
- [47] A. N. Tikhonov, V. I. Arsenin, and F. John, "The regularization method," in *Solutions of ill-posed problems*. Winston Washington, DC, 1977, vol. 14, pp. 45–94.
- [48] T. Goldstein and S. Osher, "The split bregman method for l1-regularized problems," *SIAM journal on imaging sciences*, vol. 2, no. 2, pp. 323–343, 2009.
- [49] D. Gabay and B. Mercier, "A dual algorithm for the solution of nonlinear variational problems via finite element approximation," *Computers & Mathematics with Applications*, vol. 2, no. 1, pp. 17–40, 1976.
- [50] D. P. Bertsekas and J. N. Tsitsiklis, "Augmented lagrangian methods," in *Parallel and distributed computation: numerical methods*. Prentice hall Englewood Cliffs, NJ, 1989, vol. 23, pp. 253–261.
- [51] J. Eckstein and D. P. Bertsekas, "On the douglas-rachford splitting method and the proximal point algorithm for maximal monotone operators," *Mathematical Programming*, vol. 55, no. 1, pp. 293–318, 1992.
- [52] J.-F. Cai, B. Dong, S. Osher, and Z. Shen, "Image restoration: total variation, wavelet frames, and beyond," *Journal of the American Mathematical Society*, vol. 25, no. 4, pp. 1033–1089, 2012.
- [53] D. L. Donoho, "De-noising by soft-thresholding," *IEEE Trans. Inf. Theory*, vol. 41, no. 3, pp. 613–627, 1995.
- [54] P. Mrázek and J. Weickert, "Rotationally invariant wavelet shrinkage," *Lecture notes in computer science*, pp. 156–163, 2003.
- [55] M. Chvapil, "Collagen sponge: theory and practice of medical applications," *Journal of Biomedical Materials Research Part A*, vol. 11, no. 5, pp. 721–741, 1977.
- [56] Z. Yu, F. Noo, F. Dennerlein, A. Wunderlich, G. Lauritsch, and J. Hornegger, "Simulation tools for two-dimensional experiments in x-ray computed tomography using the forbild head phantom," *Physics in medicine and biology*, vol. 57, no. 13, p. N237, 2012.
- [57] Z. Wang, A. C. Bovik, H. R. Sheikh, and E. P. Simoncelli, "Image quality assessment: from error visibility to structural similarity," *IEEE Trans. Image Process.*, vol. 13, no. 4, pp. 600–612, 2004.
- [58] A. Van der Sluis and H. Van der Vorst, "The convergence behavior of ritz values in the presence of close eigenvalues," *Linear Algebra and its Applications*, vol. 88, pp. 651–694, 1987.
- [59] Y. Liu, J. Ma, Y. Fan, and Z. Liang, "Adaptive-weighted total variation minimization for sparse data toward low-dose x-ray computed tomography image reconstruction," *Physics in medicine and biology*, vol. 57, no. 23, p. 7923, 2012.
- [60] G. M. Lasio, B. R. Whiting, and J. F. Williamson, "Statistical reconstruction for x-ray computed tomography using energy-integrating detectors," *Physics in medicine and biology*, vol. 52, no. 8, p. 2247, 2007